COMMUNICATIONS IN NUMERICAL METHODS IN ENGINEERING
Commun. Numer. Meth. Engng 2002; **18**:89–97 (DOI: 10.1002/cnm.468)

Interface tracking finite volume method for complex solid–fluid interactions on fixed meshes

H. S. Udaykumar[1,*,†], R. Mittal[2] and P. Rampunggoon[2]

[1]*Department of Mechanical Engineering, University of Iowa, Iowa City, IA 52242, U.S.A.*
[2]*Department of Mechanical Engineering, University of Florida, Gainesville, FL, U.S.A.*

SUMMARY

We present a numerical technique for computing flowfields around moving solid boundaries immersed in fixed meshes. The mixed Eulerian–Lagrangian framework treats the immersed boundaries as *sharp* solid–fluid interfaces and a conservative finite volume formulation allows boundary conditions at the moving surfaces to be exactly applied. A semi-implicit second-order accurate spatial and temporal discretization is employed with a fractional-step scheme for solving the flow equations. A multigrid accelerator for the pressure Poisson equations has been developed to apply in the presence of multiple embedded solid regions on the mesh. We present applications of the method to two types of problems: (a) solidification in the presence of flows and particles, (b) fluid–structure interactions in flow control. In both these problems, the sharp interface method presents advantages by being able to track arbitrary interface motions, while capturing the full viscous, unsteady dynamics. Copyright © 2001 John Wiley & Sons, Ltd.

KEY WORDS: moving boundary; sharp interfaces; Cartesian grid methods

1. INTRODUCTION

Our goal is to develop an algorithm that is based on a fixed mesh through which arbitrary motions of complex-shaped solid boundaries can be tracked. In previous papers, we presented the development of a methodology for simulation of diffusion-controlled growth of unstable phase boundaries [1] and fluid flow around fixed [2] and moving [3] immersed solid boundaries. In each case, we showed that the method computes the field equations to second-order accuracy, allowing capture of unsteady and viscous effects. In this paper, we provide a brief description of the method followed by applications to more challenging problems in solidification and fluid–structure interactions.

*Correspondence to: H. S. Udaykumar, Department of Mechanical Engineering, University of Iowa, 2408 Seamans Center, Iowa City, IA 52242, U.S.A.
†E-mail: ush@icaen.uiowa.edu

Contract/grant sponsor: NASA; contract/grant number: NAG-1-10124
Contract/grant sponsor: NSF CAREER; contract/grant number: Award #0092750

Copyright © 2001 John Wiley & Sons, Ltd.
Received February 2001
Accepted September 2001

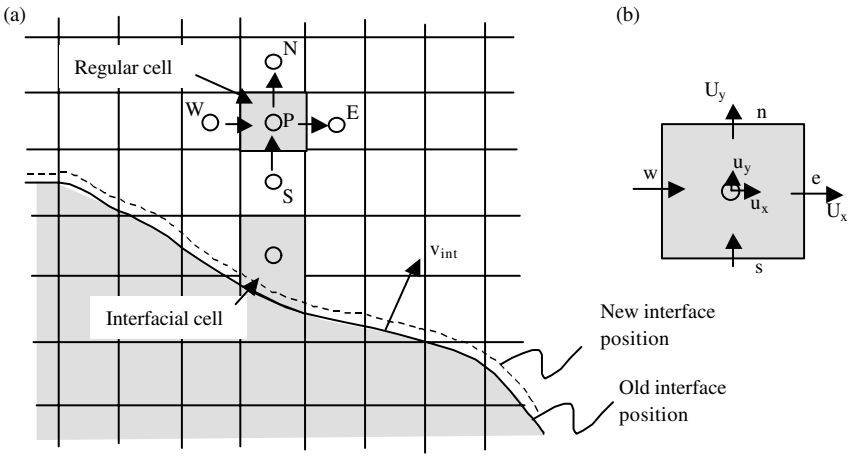

Figure 1. (a) Illustration of a moving boundary cutting through a fixed mesh. Cells traversed by the interface are called interfacial cells and are trapezoidal in shape. Cells away from the interface are regular cells; and (b) a regular cell showing the cell-face nomenclature and cell-centre and cell-face velocities.

2. THE NUMERICAL METHOD

The present method performs flow computations on a fixed Cartesian mesh, while interfaces arbitrarily travel through the mesh. Each interface is tracked using markers connected by piecewise quadratic curves parametrized by the arclength [1, 2]. In References [1, 2], we provide details regarding the interaction of the interfaces with the underlying fixed Cartesian mesh. These include obtaining locations where the interface cuts the mesh, identifying phases in which the cell centres lie, and procedures for obtaining a consistent mosaic of control volumes in the cells. This results in the formation of control-volumes near the interface which are trapezoidal in shape (see Figure 1). The finite volume discretization is then performed over these irregularly shaped cells.

The Navier–Stokes equations are discretized on the Cartesian mesh using a cell-centred colocated (non-staggered) arrangement [4] of the primitive variables. A finite-volume, fractional-step scheme [5] is employed with explicit second-order Adams–Bashforth scheme for the convective terms and implicit Crank–Nicolson scheme for the diffusion terms. The semi-discrete integral form of the advection–diffusion equation can, therefore, be written as follows:

$$St \int_v \frac{\mathbf{u}^* - \mathbf{u}^n}{\delta t}\,\mathrm{d}V = -\frac{1}{2}\oint [3\mathbf{u}^n(\mathbf{U}^n \cdot \mathbf{n}) - \mathbf{u}^{n-1}(\mathbf{U}^{n-1} \cdot \mathbf{n})]\,\mathrm{d}S$$

$$+ \frac{1}{2Re}\oint (\nabla \mathbf{u}^n + \nabla \mathbf{u}^*) \cdot \hat{n}\,\mathrm{d}S + \frac{Gr}{Re^2}\int_v (T - T_\infty)\mathbf{j}\,\mathrm{d}V \qquad (1)$$

Copyright © 2001 John Wiley & Sons, Ltd.

The continuity-enforcing step is:

$$St \int_v \frac{\mathbf{u}^{n+1} - \mathbf{u}^n}{\delta t} \, \mathrm{d}V = - \int_v \nabla p^{n+1} \, \mathrm{d}V \tag{2}$$

where $\mathbf{u}^*$ is the intermediate cell-centre velocity and $\mathbf{U}^*$ is the face-centre velocity, $\mathbf{u}$ is the non-dimensional velocity vector, p is pressure, St is the Strouhal number, a non-dimensional frequency parameter given by $St = \omega L/U_0$, $Re = U_0 L/\nu$ is the Reynolds number, $Gr = g\beta(T_m - T_\infty)R^3/\nu^2$ is the Grashof number, ω is the imposed frequency, L is the length scale, U_0 is the velocity scale, ν is the kinematic viscosity and β is the coefficient of thermal expansion.

Taking the divergence of (2) and applying Green's theorem yields the pressure Poisson equation in integral form:

$$\oint \nabla p^{n+1} \cdot \mathbf{n} \, \mathrm{d}S = \frac{St}{\delta t} \oint \mathbf{U}^* \cdot \mathbf{n} \, \mathrm{d}S \tag{3}$$

Once the pressure is obtained by solving this equation, both the cell-centre and face-centre velocities, $\mathbf{u}$ and $\mathbf{U}$ are updated separately as follows:

$$\mathbf{u}^{n+1} = \mathbf{u}^n - \delta t (\nabla p^{n+1})_{\mathrm{cc}} \tag{4}$$

$$\mathbf{U}^{n+1} = \mathbf{U}^n - \delta t (\nabla p^{n+1})_{\mathrm{fc}} \tag{5}$$

where subscripts cc and fc indicate evaluation at the cell-centre and face-centre locations, respectively.

The energy equation is solved, written in semi-discrete form as:

$$\int_v \frac{T^{n+1} - T^n}{\delta t} \, \mathrm{d}V = -\frac{1}{2} \oint [3T^n(\mathbf{U}^n \cdot \mathbf{n}) - T^{n-1}(\mathbf{U}^{n-1} \cdot \mathbf{n})] \, \mathrm{d}S + \frac{1}{2Re Pr} \oint (\nabla T^{n+1} + \nabla T^n) \cdot \hat{n} \, \mathrm{d}S \tag{6}$$

where $Pr = \nu/\alpha$ is the Prandtl number, where α is the thermal diffusivity.

The normal velocity of the moving interface is given by the physics of the problem. For phase change of pure materials, this is provided by the rate of transport of latent heat away from the solid–liquid interface (Stefan condition):

$$V_I = Ste \left(\left(\frac{\partial T}{\partial n} \right) S - \left(\frac{\partial T}{\partial n} \right) L \right) \tag{7}$$

where $Ste = \text{Stefan number} = (T_m - T_\infty)/L/C_p$ dictates the velocity of the solidification front.

For fluid–structure interaction problems [3], the velocity of the surfaces is either prescribed or computed, based on the force balance at the solid surface. The normal interfacial velocity may vary in time. It can be easily shown that this implies that $\partial p/\partial n = -St(D\mathbf{u}_\partial/Dt) \cdot \mathbf{n}_\partial$ be used as the boundary condition for Equation (3). The immersed boundary forms one side of the reconfigured boundary cells. Therefore, at that cell face the boundary conditions are

Copyright © 2001 John Wiley & Sons, Ltd.

specified. In Reference [2], we adopted a compact two-dimensional polynomial interpolating function which allows us to obtain a second-order accurate approximation of the fluxes and gradients on the faces of the trapezoidal boundary cells from available neighbouring cell-centre values. This interpolation scheme coupled with the finite-volume formulation guarantees that the accuracy and conservation property of the underlying algorithm is retained even in the presence of arbitrary-shaped immersed boundaries. This has been demonstrated in References [2, 3] for stationary and moving immersed boundaries.

The finite-volume discretization of Equations (1), (3) and (6) in a given cell P (see Reference [3]) can be written in the general form:

$$\sum_{k=1}^{M} a_k \phi_k = b \tag{8}$$

where a_k denote the coefficients accompanying the nodal values ϕ_k within a stencil consisting of M neighbours and b is the source term that contains the explicit terms as well as the terms involving boundary conditions. For cells away from the interface $M = 5$ in the central-difference spatial discretization. A multigrid technique was used to accelerate convergence of the pressure Poisson equation. Modification of a standard full approximation storage (FAS) multigrid [3] was required to take account of the presence of the immersed boundaries. In particular, the immersed boundaries was treated only at the finest grid level, and so coarsening of the geometry was not required. The discrete Laplacian operator at the coarse levels was modified to take account of the presence of the immersed boundary by using a volume-fraction approach.

The overall solution procedure with boundary motion is as follows:

1. Determine the intersection of the immersed boundary with the Cartesian mesh.
2. Using this information, reshape the boundary cells.
3. For each reshaped boundary cell, compute and store the coefficients appearing in discrete form of the Navier–Stokes equations.
4. Advance the discretized equations in time.
5. Advance the interface position in time. Go to step 1 for next time step.

3. APPLICATIONS

We now demonstrate the versatility of the numerical method by applying it to some challenging physical problems in solidification and fluid–structure interactions.

3.1. Effects of convection on dendritic growth

In real systems, such as castings, and in nature, such as in the growth of snowflakes, both forced and natural convection exert influences on the dendrite geometry and hence on the final microstructure in the solid. Therefore, it is of utmost importance to be able to quantify such convective influences on the solidification microstructure. Simulation of flow interactions with dendrites is challenging because the phase boundary grows into a complex shape and the flow needs to be computed in a geometry that changes significantly in time. In Figure 2,

Copyright © 2001 John Wiley & Sons, Ltd.

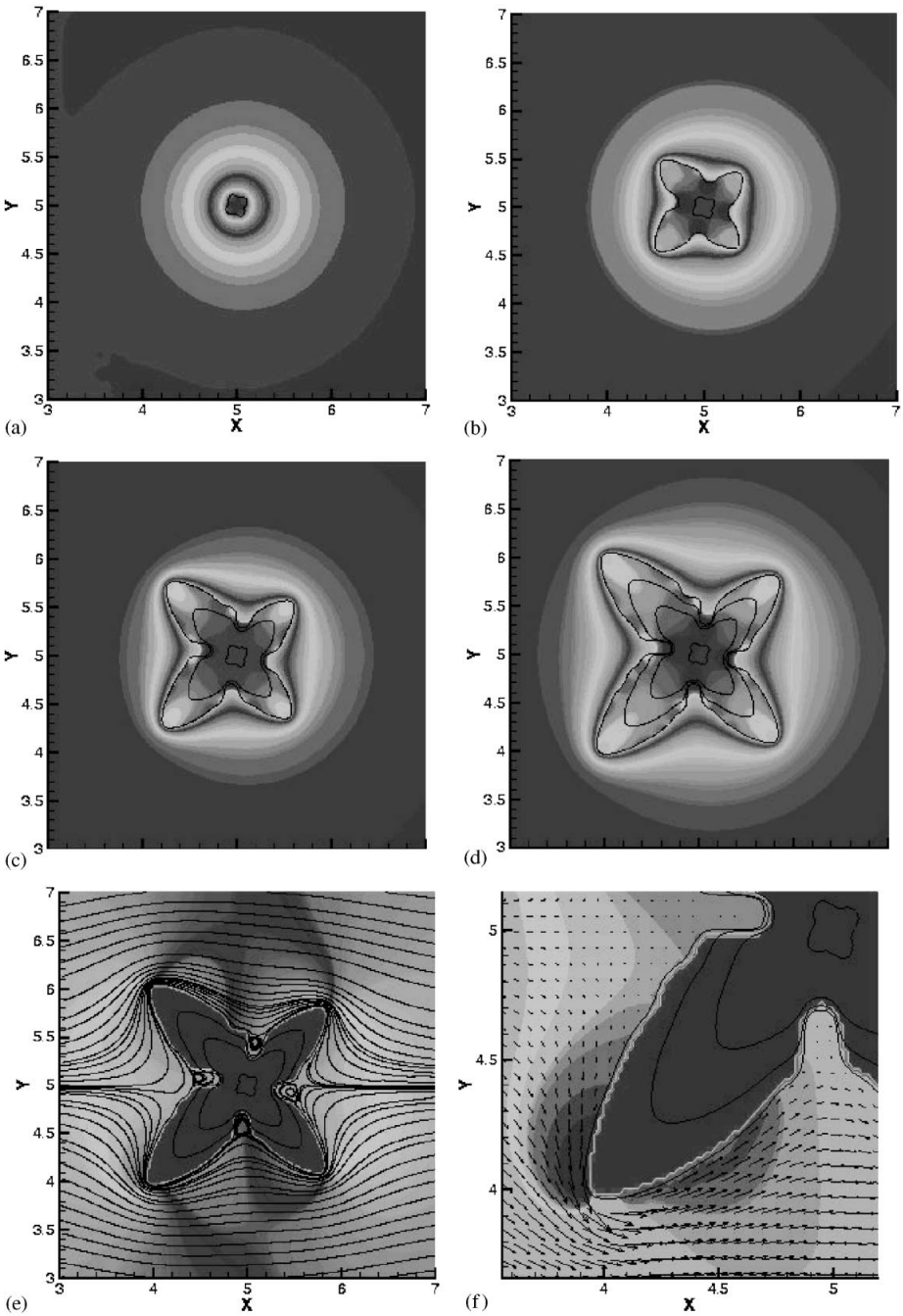

Figure 2. Simulation of flow around a growing dendrite: (a)–(d) temperature field around the growing dendrite at equal intervals of time; (e) streamlines and pressure contours for flow around the dendrite; and (f) velocity vectors around a dendrite arm. The contours in the background are of pressure. The asymmetric evolution of the dendrite shape due to convection is seen.

Copyright © 2001 John Wiley & Sons, Ltd.

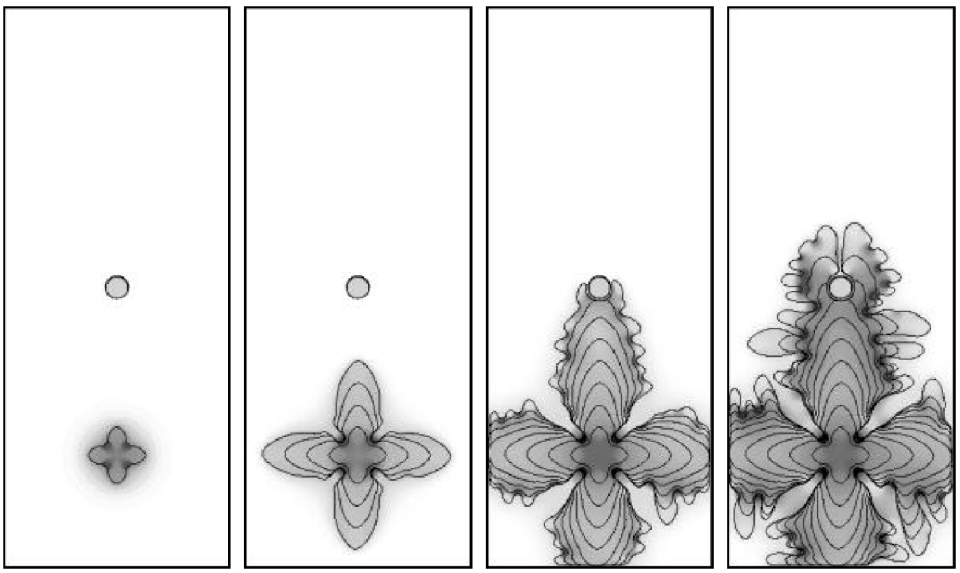

Figure 3. Calculations of dendrite–particle interaction. The seed crystal grows dendritically in the undercooled melt toward an insulated particle. The sides of the domain are adiabatic leading to latent heat trapping. Grey scales indicate hot (dark) and cold (light) regions.

we study the effect of forced convection on a growing dendrite. Flow at $Re = 1.0$ enters at the left boundary and leaves at the right boundary. The shapes of the dendrite are shown at four instants in the growth. The melt was initially at uniform temperature of $T = -0.8$, and the solid was at $T = 0.0$. In time, the diffusion of latent heat forms a thermal boundary layer with thickness of order (α_l/V_I) in the liquid. The effect of forced convection is clearly seen in that the dendrite arms facing the oncoming flow grow much faster than the arms on the downstream side. This is due to the compression of the thermal boundary layer on the upstream side. This behaviour agrees with experiments [6–8] and diffuse interface simulation [9]. Figure 2(e, f) shows the details of the flowfield around the mature dendrite. The contours in Figure 2(e, f) show the pressure field around the dendrite.

3.2. Interaction of complex solidification fronts with particles

In Figure 3, we show the growth of a dendritic front from an initial seed and study its evolution as it approaches a stationary insulated particle placed some distance away in the melt. Such dendrite–particle interactions are important to understand to effect better microstructural control in the manufacture of advanced metal–matrix composites (MMCs) [10]. In the computed example, the melt is pure, undercooled ($Ste = -0.8$), the sides of the domain are adiabatic. In the case shown, the dendrite arm facing the bulk melt grows steadily as expected from theory, with a parabolic tip of constant radius. The grey scale shows the temperature distribution, darker shades implying hotter regions. The troughs of side-branches are dark due to the capillarity effect (Gibbs–Thomson condition) and the accumulation of latent heat in

Copyright © 2001 John Wiley & Sons, Ltd.

the grooves. The thermal boundary layer is thin, causing the tip to approach the insulated particle very closely before it 'feels' the particle. Because the particle is insulated, the latent heat accumulates between the particle and the tip, and a gap develops between the front and the particle, as clearly shown here. Note that in MMCs, the ceramic inserts typically have lower conductivity than the metal melt (e.g. $K_p(SiO_2)/K_l(Al) = 0.35$) and hence the development of a trough is expected there as seen in experiments [11]. Contact with the particle splits the dendrite tip in agreement with experiments [12]. This appears to set off profuse side-branching, and the wavelength of the side-branches near the particle is seen to be shorter (perhaps due to the sharper tip of the split dendrite as it goes around the particle). However, this behaviour may be sensitive to the ratio of particle radius (R_p) to dendrite tip radius (R_{tip}). This type of microstructural length scale modification, including grain refining by the particles is observed in experiments [10, 12]. Away from the particle, the dendrite appears to grow with the usual coarsening mode of evolution. In this case, the stationary particle has been engulfed by the solidifying front; mobile particles and pushing effects are now being studied.

3.3. Simulation of a synthetic jet actuator

The synthetic jet has emerged as one of the most useful microfluidic devices with potential applications ranging from thrust vectoring of jet engines to active control of separation and turbulence in boundary layers [13, 14]. The performance characteristics of a synthetic jet actuator depends on a number of geometrical, structural and flow parameters and there is little understanding as to how the performance characteristics scale with these parameters [15]. A schematic of a model of a diaphragm-driven synthetic jet actuator for boundary layer control is shown in Figure 4(a). The diaphragm oscillates sinusoidally in time and also has a sinusoidal variation in space. The flow has been simulated on a non-uniform Cartesian mesh and the entire synthetic jet cavity including the oscillating diaphragm is represented using the technique described above. Figures 4(b–d) show spanwise vorticity plots for three different cases, corresponding to $Re_\delta = 0, 1200$ and 2600, respectively, where Re_δ is the Reynolds number of the external boundary layer defined based on the freestream velocity and boundary layer thickness. The plots clearly show the variation in effectiveness of the actuator observed with increasing Reynolds number. While for very low Reynolds numbers, the vortices generated at the cavity lip penetrates the boundary layer and are hence ineffective, at very high Reynolds numbers, due to the strength of the cross-flow, the synthetic jet is unable to heavily influence the boundary layer thickness. Simulation of flow over one oscillation of the diaphragm requires roughly 5 CPU h on a 750 MHZ DEC-Alpha, UNIX workstation demonstrating the ease with which this relatively complex flow can be simulated using the current methodology.

4. SUMMARY

We have developed a numerical method for the computation of fluid flow and thermal transport in the presence of moving solid boundaries. Freeing the mesh from conforming to the often complex evolving boundaries while maintaining a sharp solid–liquid interface allows for the accurate solution of a wide range of phase change and fluid–structure interaction problems.

Copyright © 2001 John Wiley & Sons, Ltd.

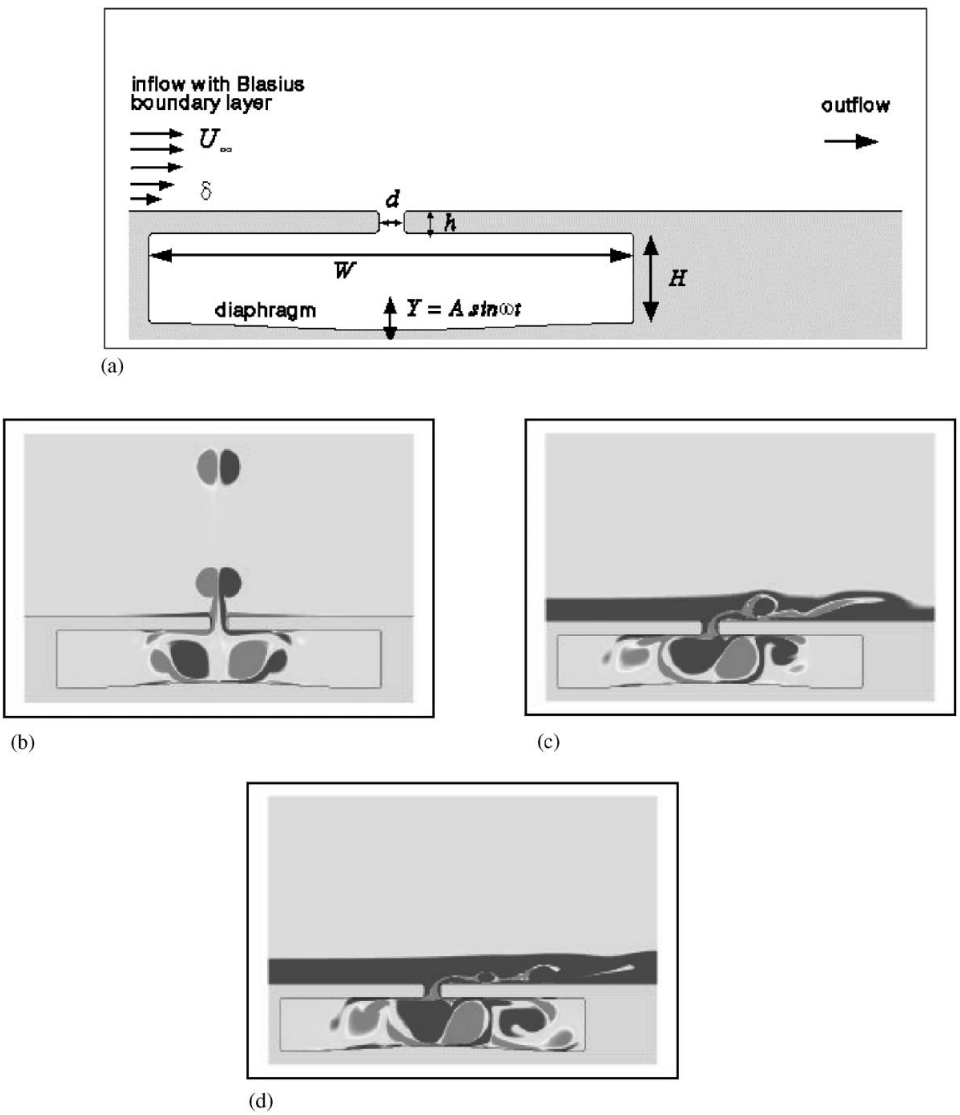

Figure 4. (a) Schematic of the synthetic jet configuration for boundary layer control. Vorticity contour for; (b) $Re = 0$, for a particular position of the diaphragm; (c) $Re = 1200$ at the same instant; and (d) $Re = 2600$ for that instant.

We have applied the method to two challenging problems, namely the dynamics of growing dendrites in the presence of fluid flow and embedded particles and fluid–structure interactions in flow control. Both problems demand the solution of viscous, unsteady flows with accurate capture of boundary layers (momentum and thermal). The sharp interface nature and the second-order spatial and temporal discretization coupled with a conservative finite volume scheme allows us to accurately compute the interfacial dynamics.

Copyright © 2001 John Wiley & Sons, Ltd.

ACKNOWLEDGEMENTS

RM would like to acknowledge support from NASA under Grant NAG-1-10124 monitored by Susan Gorton. HSU acknowledges partial support from NSF CAREER program (CTS Division) via Award#0092750.

REFERENCES

1. Udaykumar HS, Mittal R, Shyy W. Solid–liquid phase front computations in the sharp interface limit on fixed grids. *Journal of Computational Physics* 1999; **153**:535–574.
2. Ye T, Mittal R, Udaykumar HS, Shyy W. An accurate Cartesian grid method for viscous incompressible flows with complex immersed boundaries. *Journal of Computational Physics* 1999; **156**:209–240.
3. Udaykumar HS, Mittal R, Rampunggoon P, Khanna A. A sharp interface Cartesian grid method for simulating flows with complex moving boundaries. *Journal of Computational Physics* 2001; **174**:1–36.
4. Zang Y, Street RL, Koseff JR. A non-staggered grid, fractional step method for time-dependent incompressible Navier–Stokes equations in curvilinear coordinates. *Journal of Computational Physics* 1994; **114**:18.
5. Chorin AJ. Numerical solution of the Navier–Stokes equations. *Mathematics of Computation* 1968; **22**:745.
6. McCay TD, McCay MH. Measured and predicted effects of gravity level on directional dendritic solidification of NH4Cl-H20. *Microgravity Science and Technology* 1993; **I**/**1**:2–12.
7. Kallungal JP, Barduhn AJ. Growth rate of an ice crystal in subcooled pure water. *A.I.Ch.E. Journal* 1997; **23**(3):294–303.
8. Glicksman ME, Huang SC. In *Convective Transport and Instability Phenomena*, Zierep J, Oertel H (eds.). Karlsruhe: Braun, 1982; 3.2.2.
9. Tong X, Beckermann C, Karma A. Velocity and shape selection of dendritic crystals in a forced flow. *Physics Review E* 2000; **61**:R49–R52.
10. Rohatgi PK, Asthana R, Das S. Solidification, structures, and properties of cast metal–ceramic particle composites. *International Materials Review* 1986; **31**:115–139.
11. Sen S, Kaukler WF, Curreri P, Stefanescu DM. Dynamics of solid/liquid interface shape evolution near an insoluble particle—an X-ray transmission microscopy investigation. *Metallurgist and Materials Transactions* 1997; **28A**:2129–2135.
12. Sekhar JA, Trivedi R. Solidification interface configurations during the processing of particulate composites. In *Solidification of Metal Matrix Composites*, TMS, Rohatgi P (ed.). 1989.
13. Smith BL, Glezer A. The formation and evolution of synthetic jets. *Physics of Fluids* 1998; **10**(9):2281–2289.
14. Crook A, Sadri AM, Wood NJ. The development and implementation of synthetic jets for the control of separated flow. *AIAA* 9-3176, 1999.
15. Rampunggoon P, Mittal R, Udaykumar HS, Cattafesta L. Numerical investigation of the interaction of a synthetic jet with a flat plate boundary layer. *Bulletin of the American Physical Society* November 2000; vol. 45 no.9.

Copyright © 2001 John Wiley & Sons, Ltd.